The Astrophysical Journal Letters, 957:L5 (10pp), 2023 November 1 https://doi.org/10.3847/2041-8213/ad0130

Pavo: Discovery of a Star-forming Dwarf Galaxy Just Outside the Local Group*

Michael G. Jones[1], Burçin Mutlu-Pakdil[2], David J. Sand[1], Richard Donnerstein[1], Denija Crnojević[3], Paul Bennet[4], Catherine E. Fielder[1], Ananthan Karunakaran[5,6], Kristine Spekkens[7,8], Jay Strader[9], Ryan Urquhart[9], and Dennis Zaritsky[1]
[1] Steward Observatory, University of Arizona, 933 North Cherry Avenue, Room N204, Tucson, AZ 85721-0065, USA; jonesmg@arizona.edu
[2] Department of Physics and Astronomy, Dartmouth College, Hanover, NH 03755, USA
[3] University of Tampa, 401 West Kennedy Boulevard, Tampa, FL 33606, USA
[4] Space Telescope Science Institute, 3700 San Martin Drive, Baltimore, MD 21218, USA
[5] Department of Astronomy & Astrophysics, University of Toronto, Toronto, ON M5S 3H4, Canada
[6] Dunlap Institute for Astronomy and Astrophysics, University of Toronto, Toronto ON, M5S 3H4, Canada
[7] Department of Physics and Space Science, Royal Military College of Canada, P.O. Box 17000, Station Forces Kingston, ON K7K 7B4, Canada
[8] Department of Physics, Engineering Physics and Astronomy, Queen's University, Kingston, ON K7L 3N6, Canada
[9] Center for Data Intensive and Time Domain Astronomy, Department of Physics and Astronomy, Michigan State University, East Lansing, MI 48824, USA
Received 2023 October 1; revised 2023 October 6; accepted 2023 October 7; published 2023 October 25

Abstract

We report the discovery of Pavo, a faint ($M_V = -10.0$), star-forming, irregular, and extremely isolated dwarf galaxy at $D \approx 2$ Mpc. Pavo was identified in Dark Energy Camera Legacy Survey imaging via a novel approach that combines low surface brightness galaxy search algorithms and machine-learning candidate classifications. Follow-up imaging with the Inamori-Magellan Areal Camera and Spectrograph on the 6.5 m Magellan Baade telescope revealed a color–magnitude diagram (CMD) with an old stellar population, in addition to the young population that dominates the integrated light, and a tip of the red giant branch distance estimate of $1.99^{+0.20}_{-0.22}$ Mpc. The blue population of stars in the CMD is consistent with the youngest stars having formed no later than 150 Myr ago. We also detected no Hα emission with SOAR telescope imaging, suggesting that we may be witnessing a temporary low in Pavo's star formation. We estimate the total stellar mass of Pavo to be $\log M_*/M_\odot = 5.6 \pm 0.2$ and measure an upper limit on its H I gas mass of 1.0×10^6 $M_\odot$ based on the HIPASS survey. Given these properties, Pavo's closest analog is Leo P ($D = 1.6$ Mpc), previously the only known isolated, star-forming, Local Volume dwarf galaxy in this mass range. However, Pavo appears to be even more isolated, with no other known galaxy residing within over 600 kpc. As surveys and search techniques continue to improve, we anticipate an entire population of analogous objects being detected just outside the Local Group.

Unified Astronomy Thesaurus concepts: Dwarf irregular galaxies (417); Low surface brightness galaxies (940); Galaxy stellar content (621); Galaxy environments (2029); Galaxy distances (590)

1. Introduction

Galaxies at the extremely low mass end ($M_* \lesssim 10^6$ $M_\odot$) of the population offer unique tests of our understanding of galaxy evolution and cosmology (e.g., Bullock & Boylan-Kolchin 2017; Sales et al. 2022). With the rise of cosmological simulations over the past few decades, several high-profile discrepancies between the number and form of low-mass galaxies in these simulations and those observed in the Local Volume came to light (Moore 1994; Klypin et al. 1999; Boylan-Kolchin et al. 2011; McGaugh 2012; Pawlowski et al. 2012). The inclusion of additional astrophysics in increasingly high resolution simulations (e.g., Brook & Di Cintio 2015; Dutton et al. 2016; Sawala et al. 2016; Wetzel et al. 2016; Garrison-Kimmel et al. 2017) and the continued discovery of more nearby low-mass galaxies with improved surveys (e.g., Willman et al. 2005; Belokurov et al. 2006; Irwin et al. 2007; McConnachie et al. 2008; Drlica-Wagner et al. 2015; Koposov et al. 2015; Cerny et al. 2021; Collins et al. 2022) have offered resolutions to most of these issues. However, our understanding of the very lowest mass galaxies, especially beyond the influence of the Milky Way (MW) and M31, remains quite limited. In particular, current cosmological models predict that galaxies below a certain mass threshold will be permanently quenched by cosmic reionization (Benson et al. 2002; Bovill & Ricotti 2009; Simpson et al. 2013; Wheeler et al. 2015; Fitts et al. 2017), but this characteristic mass threshold is still largely unconstrained observationally (see Simon 2019, for a review).

Resolved star searches with the Sloan Digital Sky Survey (SDSS; York et al. 2000), the Dark Energy Survey (Sánchez & Des Collaboration 2010), the Dark Energy Camera Legacy Survey (DECaLS; Dey et al. 2019), and the DECam Local Volume Exploration survey (Drlica-Wagner et al. 2021) led to a flurry of ultrafaint dwarf (UFD)[10] discoveries in (or just outside) the Local Group (LG; e.g., Willman et al. 2005; Belokurov et al. 2006; Drlica-Wagner et al. 2015; Koposov et al. 2015; Collins et al. 2022; Martínez-Delgado et al. 2022; Sand et al. 2022; Cerny et al. 2023; McQuinn et al. 2023), while focused deep-imaging projects identified small samples of faint dwarfs in other nearby groups (e.g., Chiboucas et al. 2013; Crnojević et al. 2014, 2016; Carlin et al. 2016, 2021; Smercina et al. 2017, 2018; Bennet et al. 2019; Müller et al. 2019; Mutlu-Pakdil et al. 2022; McNanna et al. 2023). In the

* This paper includes data gathered with the 6.5 m Magellan Telescope at Las Campanas Observatory, Chile.

[10] Generally, dwarfs fainter than $M_V = -7.7$ ($M_* \lesssim 10^5$ $M_\odot$) are considered to be UFDs (e.g., Simon 2019).

case of star-forming galaxies, many of the currently known lowest-mass galaxies were identified through their H I emission in the Arecibo Legacy Fast ALFA (ALFALFA; Giovanelli et al. 2005; Haynes et al. 2018) survey and the Study of H I In Extremely Low-mass Dwarfs (SHIELD; Cannon et al. 2011).

Isolated galaxies at the lowest masses are of particular interest, as they sample one of the extremes of what constitutes a galaxy, while their isolation provides a clean environment in which to study their nature in the absence of influence from other, more massive galaxies. At present, two of the lowest-mass galaxies known in relative isolation are Leo P, $\log L_V/L_* = 5.7$ (Giovanelli et al. 2013; McQuinn et al. 2015b), and Tucana B, $\log L_V/L_* = 4.7$ (Sand et al. 2022), with the former being star-forming and the latter quenched. Throughout this work, we will use these two objects as points of comparison, as they appear to bridge the threshold that determines whether or not a galaxy was quenched by cosmic reionization.

The stellar mass of Leo P is roughly 10 times higher than that of Tucana B (and roughly half of Leo P's baryonic mass is in neutral gas), and in general, the lowest (stellar) mass galaxies in the SHIELD sample are roughly an order of magnitude above the most massive UFDs (McQuinn et al. 2014). Thus, there is a disconnect between the lowest-mass star-forming galaxies known in the field and UFDs thought to be quenched by reionization. With suitably modified search techniques and the inclusion of machine learning, it is likely that existing imaging surveys can be used to begin to fill this gap and connect these two populations. There are likely many Tucana B and Leo P analogs just outside the LG, where they would appear as semiresolved objects in existing ground-based, wide-field imaging surveys. This is a regime where current search algorithms perform poorly (e.g., Mutlu-Pakdil et al. 2021). In this letter, we briefly discuss a novel approach to identifying these objects and present the first notable discovery from our search.

2. Search and Discovery

Starting with publicly available images from the DR10 of the Dark Energy Spectroscopic Instrument (DESI) legacy imaging surveys (Dey et al. 2019), DECaLS, the Mayall z-band Legacy Survey (MzLS), and the Beijing–Arizona Sky Survey (BASS), we have used a modified version of the Systematically Measuring Ultra-Diffuse Galaxies (SMUDGes; Zaritsky et al. 2019), pipeline as well as retraining its neural network classifier to identify both UFD and SHIELD-like objects. Here we give a brief overview of the search process. Full details of the SMUDGes pipeline can be found in the original publications (Zaritsky et al. 2019, 2021, 2022, 2023), and a more complete description of our search will be presented in subsequent papers covering all candidate objects.

The original SMUDGes pipeline used images from individual exposures but switched to using the Legacy Survey bricks for the northern survey area. For simplicity and speed, we also chose to adopt the latter strategy. The pipeline starts by identifying high surface brightness objects, subtracting them, and replacing them with characteristic noise. A range of wavelet-filtering scales were then used to identify candidates. Candidates must be detected in at least two bands, separated by less than 4″. The light profiles of the initial candidates were fit with `GALFIT` (Peng et al. 2002, 2010) using a forced exponential profile. Using the criteria described in Zaritsky et al. (2023), several cuts were then applied: $r_e > 4''$, $b/a > 0.34$, and $\mu_{0,g} > 22.5$ mag arcsec^{-2}, or $\mu_{0,z} > 21.5$ mag arcsec^{-2} where the g band was unavailable. These cuts were originally designed to eliminate some of the large number of spurious objects picked up by the wavelet filtering while remaining generous enough to avoid rejecting candidates that would pass a second round of fitting with full Sérsic profiles (a more computationally intensive step). However, in practice, no further cuts were needed after the second round of `GALFIT` fitting (with a free Sérsic index) before beginning to classify the candidates.

These steps produced a sample of approximately 4×10^5 candidates over the full Legacy Survey DR10. We began by visually inspecting all candidates within an $\sim$300 deg^2 pilot area and classifying them as either candidate nearby (semi) resolved galaxies (our target objects), other types of galaxies (not the targets of this search), or spurious detections (e.g., distant galaxy groups or Galactic cirrus). The SMUDGes convolutional neural network (CNN) image classifier was then retrained with g, r, and z fits cutouts ($\sim 88'' \times 88''$) of known UFDs, Local Volume dwarf galaxies, the nearest SHIELD galaxies, low-luminosity globular clusters within the LG, and high-confidence candidates from the pilot search. The spurious candidates were also added to the training set as negative examples. A second pilot area of $\sim$150 deg^2 near the Galactic plane was used to test the level of contamination from Galactic cirrus. This led to a second round of training containing many examples of unwanted cirrus features.

A total of 3933 candidates were given a >90% probability of being (semi)resolved nearby galaxies by the CNN classifier, a factor of $\sim$100 reduction from the initial catalog of candidates.[11] After an initial visual screening for spurious candidates that made it past the CNN (mostly cirrus, background galaxy groups, spiral arms, or tidal structures), cutouts of 1314 candidates were uploaded to the `Zooniverse` platform,[12] where six volunteers from our team classified them as in the pilot search discussed above. A total of 321 of these candidates were classified by at least one volunteer as likely being nearby, low-mass (semi)resolved galaxies and therefore flagged for further investigation. The majority of these objects are known nearby galaxies; however, roughly a quarter are entirely uncataloged.

One striking example is shown in Figure 1: a blue, irregular dwarf galaxy reminiscent of Leo P. Upon inspection, it was immediately realized that this is likely a very nearby object due to its extended and clearly semiresolved appearance in the ground-based DECaLS imaging. We named this object "Pavo" after the constellation in which it resides.

3. Follow-up Observations

3.1. Magellan Baade Imaging

To further understand the physical and star formation properties of Pavo, we obtained deep g- and r-band imaging with the Inamori-Magellan Areal Camera and Spectrograph (IMACS; Dressler et al. 2006) on the Magellan Baade 6.5 m telescope on 2023 July 14 (UT). We used the $f/2$ camera, which has an $\sim$27.′4 field of view and 0.″2 pixel^{-1} scale. We took 11×300 s exposures in the g band and 11×300 s exposures in the r band, with small dithers in between exposures. The data were reduced in a standard way (as in Chiti et al. 2020) with standard image

[11] In the case of MzLS/BASS, we performed Gaussian smoothing with a 1.5 pixel kernel to reduce noise before passing the candidate cutouts to the CNN. A threshold probability of 98% was also used for MzLS/BASS (instead of 90%) to reduce the number of false-positive candidates.

[12] www.zooniverse.org

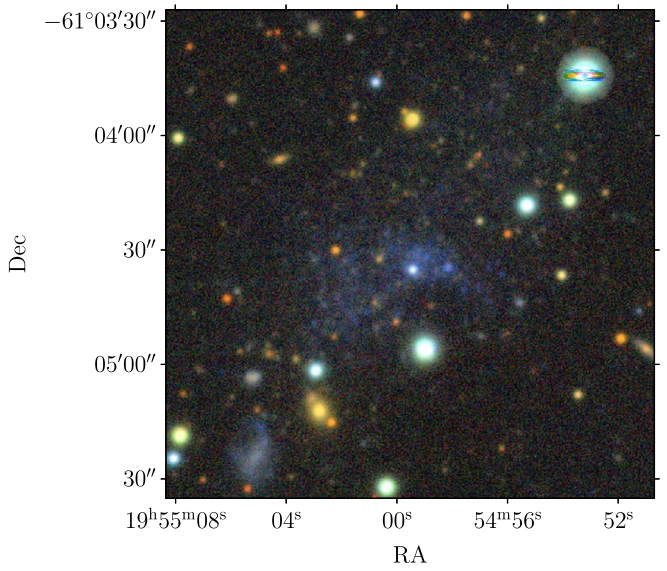

Figure 1. DECaLS DR10 *gri* cutout of Pavo, similar to that used for the original classification.

detrending. Astrometric correction was a two-step process, with an initial world coordinate system solution supplied by `astrometry.net` (Lang et al. 2010), followed by a refined solution computed by `SCAMP` (Bertin 2006). Final image stacking used the `SWarp` (Bertin et al. 2002) software package, using a weighted average of the input images. The final stacked images have point-spread function FWHM values of 0.″9 in both the g and r bands.

Point-source photometry was performed on the stacked IMACS images using the `daophot` and `allframe` software suite (Stetson 1987, 1994), similar to that described in Mutlu-Pakdil et al. (2018). We removed objects that are not point sources by culling our `allframe` catalog of outliers in χ[13] versus magnitude, magnitude error versus magnitude, and sharpness versus magnitude space. We calibrated the photometry by matching it to the Legacy Survey DR10. We corrected for MW extinction on a star-by-star basis using the Schlegel et al. (1998) reddening maps with the coefficients from Schlafly & Finkbeiner (2011). The extinction-corrected photometry is used throughout this work.

We perform a series of artificial star tests with the `daophot` routine `addstar` to determine our photometric errors and completeness as a function of magnitude and color. Similar to Mutlu-Pakdil et al. (2018), we placed artificial stars into our images on a regular grid (1020 times the image FWHM). Ten iterations are performed on the image for a total of ∼100,000 artificial stars each. These images are then photometered in the same way as the unaltered image stacks, and the same stellar selection criteria on χ, magnitude, magnitude error, and sharpness were applied to the artificial star catalogs to determine completeness and magnitude uncertainties. The 50% (90%) completeness level is at $r = 26.5$ (24.5) and $g = 27.0$ (24.5) mag.

3.2. SOAR Hα Imaging

To look for sites of ongoing star formation, an Hα image of Pavo was obtained with the 4.1 m Southern Astrophysical Research (SOAR) telescope on 2023 September 17 with the Goodman Spectrograph (Clemens et al. 2004). The narrowband Hα filter has a central wavelength of 6563 Å and a width of 75 Å. The SDSS r-band filter was used for the continuum image. Pavo was observed with a three-point dither in both filters for total exposure times of 1800 s (Hα) and 180 s (r). Images were binned 2 × 2 to give a pixel scale of 0.″3 pixel^{-1}.

Images were reduced using `ccdproc`. Individual exposures were aligned with `astroalign` before median stacking, and the final world coordinate system was derived with `astrometry.net`. Stars were extracted from both the r-band and Hα images, and a linear fit to the relation between their fluxes was used to scale the r-band image and subtract the continuum. The continuum subtraction removed the entirety of Pavo from the Hα image, indicating that there are no sites of significant Hα emission (i.e., H II regions).

Table 1
Properties of Pavo

Parameter	Value
R.A.	19:54:59.″98 ± 7.″9
Decl.	−61:04:20.″5 ± 5.″8
m_g(mag)	16.7 ± 0.1
m_r(mag)	16.4 ± 0.1
m_i(mag)	16.3 ± 0.1
m_z(mag)	16.1 ± 0.1
Dist. (Mpc)	$1.99^{+0.20}_{-0.22}$
M_V (mag)	−10.0 ± 0.1
r_h	1.′25 ± 0.′10
r_h (pc)	713 ± 57
ϵ	0.51 ± 0.08
θ	131° ± 21°
$\log(\mathrm{SFR_{UV}}/M_\odot\ \mathrm{yr}^{-1})$	$-4.0^{+0.3}_{-0.8}$
$\log M_*$ ($M_\odot$)	5.6 ± 0.2
$\log M_{\mathrm{H\,I}}$ ($M_\odot$)	<6.0

Note. Stated uncertainties of distance-dependent quantities do not include the contribution from the distance uncertainty.

3.3. Swift Observations

Pavo lies in a gap in the Galaxy Evolution Explorer (GALEX) all-sky imaging survey, and we therefore obtained UV imaging from the NASA Neil Gehrels Swift observatory in all three UV bands (UVW1, UVM2, and UVW2). Pavo was observed over two sequences on 2023 September 19 and 20. Unfortunately, the sequence taken on 2023 September 19 was unusable due to a detector artifact produced by a bright star, leaving only the 2023 September 20 sequence. Pavo was detected in all three bands; however, due to its color similarity to the GALEX near-UV (NUV), we use only the UVM2 filter to determine the star formation rate (SFR; Hoversten et al. 2009). We measure the flux from Pavo using an aperture based on double the optical half-light radius, masking contaminating sources such as bright stars in this region. The measured flux is very close to the zero-point for the Ultra-Violet Optical Telescope (UVOT); therefore, the uncertainty on the measured flux is high. The raw flux was corrected for foreground extinction and sensitivity loss following the UVOT calibration documents. We then color-corrected the UVOT flux to GALEX NUV and used the relation from Iglesias-Páramo et al. (2006) to derive an SFR (Table 1).

[13] Here χ is a measure of the quality of the fit between the model and the actual stars in the image.

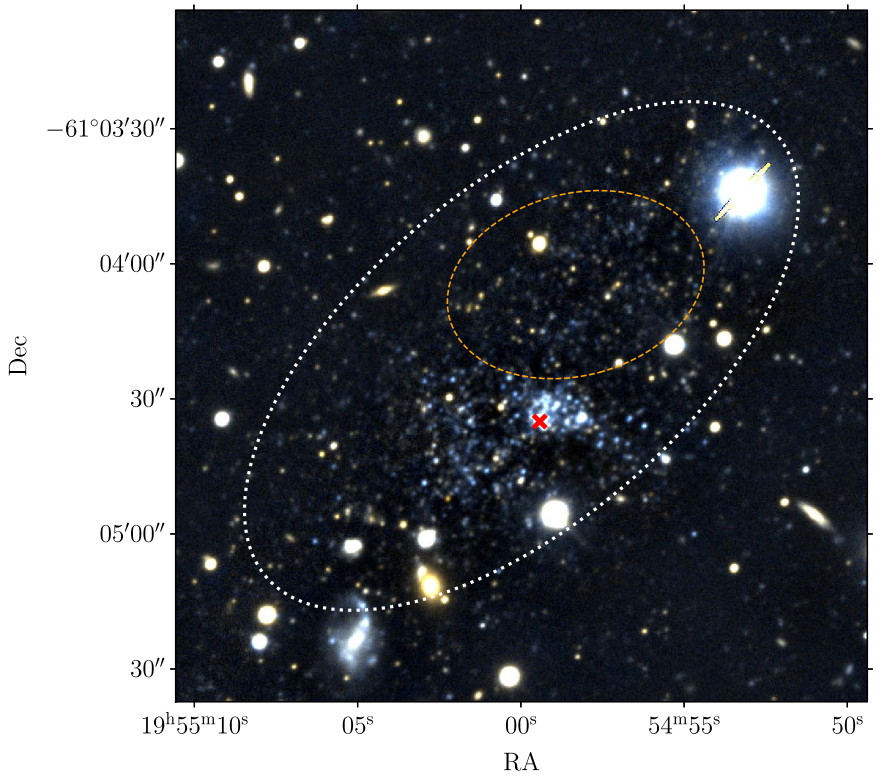

Figure 2. IMACS $g + r$ color image of Pavo. The central and SE portions of its irregular stellar body are dominated by blue stars, but it also extends to the NW, where older, redder stars become the dominant population. The white dotted ellipse shows the region used to produce the full CMD of Pavo (Figure 3, top left), and the orange dashed ellipse shows the region dominated by redder stars (Figure 3, top right). The field contains many foreground stars, and the apparent central cluster of Pavo is actually a superimposed foreground star with detectable proper motion. We have marked this star with a red cross.

4. Properties of Pavo

4.1. Color and Morphology

The DECaLS image of Pavo is dominated by its young, blue stellar component, which extends from the center of Figure 1 to the SE. It has a highly speckled appearance indicating that the stellar population is only slightly too distant to be resolved into individual stars. The distribution of blue stars is also highly irregular, with no clear ordered structure or center. Prior to the SOAR Hα observations (and the nondetection of Pavo), the brightest clump near the center of the image was considered as a possible star cluster or H II region. However, this object was identified as having measurable proper motion (7.2 mas yr^{-1}) in the Gaia survey (Gaia Collaboration et al. 2016, 2023) and is therefore a foreground star. Bailer-Jones et al. (2021) estimated the distance to this star as $3.0^{+1.5}_{-1.0}$ kpc. It is marked with a red cross in Figure 2.

The IMACS image of Pavo (Figure 2) resolves the stellar population, revealing that, in addition to the blue stars seen in the DECaLS image in the SE, an older, redder population extends to the NW. This is likely the underlying stellar population of the galaxy, whereas the seemingly dominant blue population only represents the most recent star formation. Star formation is highly stochastic in low-mass galaxies (e.g., McQuinn et al. 2015a); thus, the blue population that dominates the total integrated light can give a very misleading impression of the underlying structure (see Section 4.3).

These findings indicate that Pavo hosts both an old stellar population and a recently formed one. It therefore cannot be a transient object and is instead a long-lived, bona fide dwarf galaxy, albeit at a very low mass. It must also have recently contained enough gas to ignite a recent episode of star formation. It may have been continuously forming stars (perhaps with bursts and lulls) for much of its lifetime, or it may have only recently begun to form stars again after a long quiescent period. We will revisit this point and discuss the nature of its stellar population in Section 4.4.

4.2. Distance

We derive the distance to Pavo via the tip of the red giant branch (TRGB) method (e.g., Da Costa & Armandroff 1990; Lee et al. 1993; Makarov et al. 2006), where the sharp discontinuity at the bright end of an old red giant branch (RGB) population is used as a standard candle. To perform the measurement, we only consider the NW region of the galaxy (see Figure 3), in order to have as little contamination as possible from the young, massive stars in Pavo; we additionally apply a color cut of $g - r < 1.35$ to avoid foreground contaminants. We derive the luminosity function for the RGB stars and fit it with a model luminosity function after having convolved the latter with the photometric uncertainty, bias, and completeness as derived from our artificial star tests (see Crnojević et al. 2019 for details). The nonlinear least-squares fitting returns a value of $r_{\rm TRGB} = 23.48 \pm 0.21$ for the TRGB magnitude. This translates into a distance modulus of $(m - M) = 26.49 \pm 0.23$ mag, or a distance of $1.99^{+0.20}_{-0.22}$ Mpc, according to the TRGB calibration in the SDSS bands derived by Sand et al. (2014), $M_r^{\rm TRGB} = -3.01 \pm 0.10$. An old, metal-poor RGB isochrone from the PAdova and TRieste Stellar Evolution Code (PARSEC; Bressan et al. 2012) scaled to this distance is overlaid on a binned version of the color–magnitude diagram (CMD) in the bottom middle panel of Figure 3.

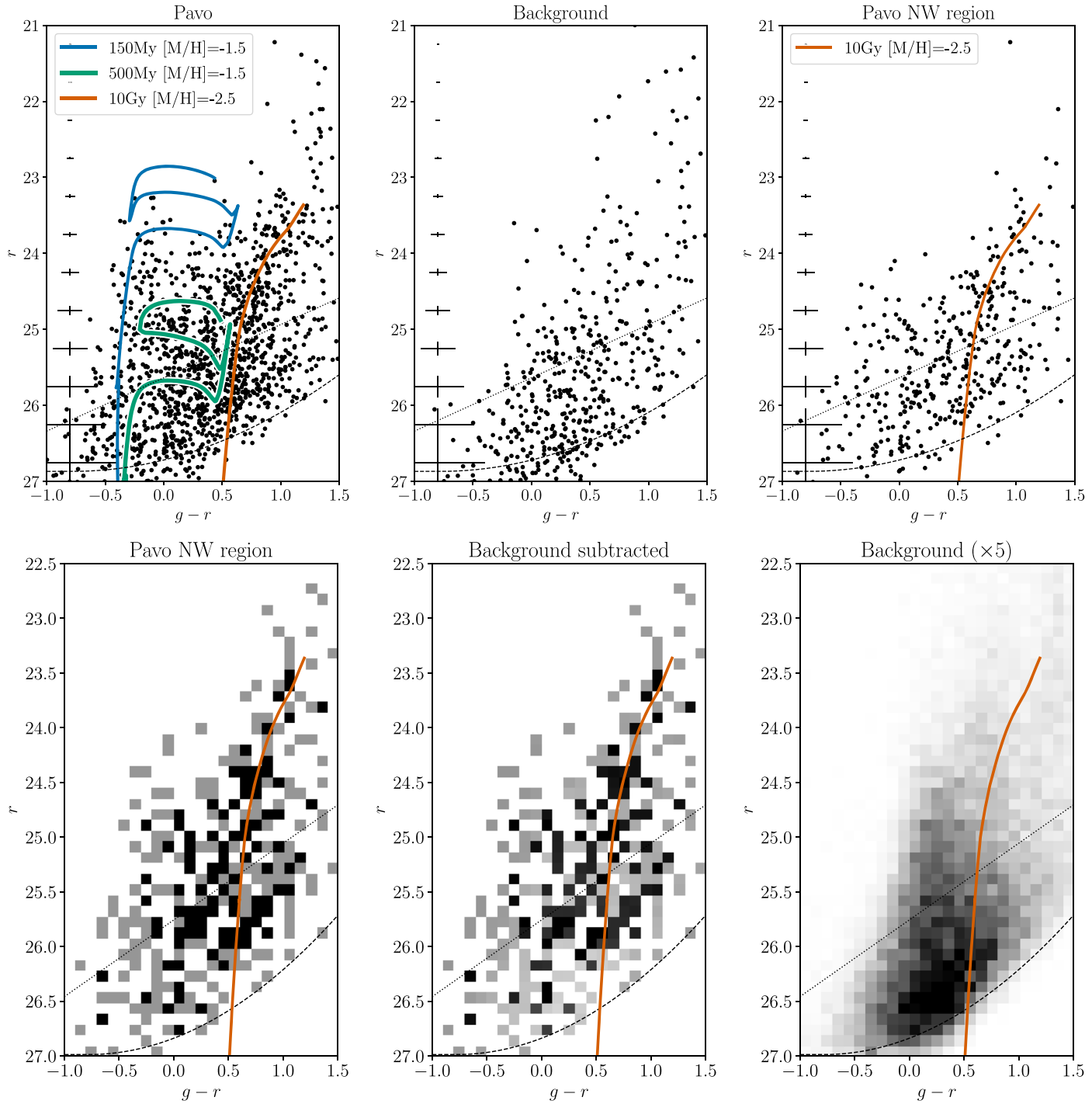

Figure 3. Top left: CMD of the stellar population of Pavo from the IMACS imaging. The blue and green isochrones indicate the main-sequence and HeB phases of 150 and 500 Myr old populations, respectively. The metallicity in both cases is set to [M/H] = −1.5 to roughly match that of Leo P. The orange isochrone shows the location of an ancient and metal-poor (10 Gyr and [M/H] = −2.5) RGB. Top middle: background CMD created by downsampling the CMD of the full field of view (minus the region containing Pavo) to an area equal to the white dotted ellipse in Figure 2. Top right: CMD of the stellar population within the orange dashed ellipse (Figure 2). The RGB isochrone from the left panel is reproduced here. In all three top panels, the dashed line indicates the 50% completeness limit, the dotted line indicates the 90% limit, and the error bars on the left indicate the typical photometric uncertainties in bins of 0.5 mag in the *r* band. Bottom left: binned version of the CMD of the NW region of Pavo (0.1 mag bins). Bottom middle: same CMD with the background contribution subtracted. Bottom right: binned CMD of the background over the entire field of view (with Pavo excluded), weighted by five times the area of the region used in the bottom left and middle CMDs (to make it more clearly visible on the same scale). The 10 Gyr, [M/H] = −2.5 PARSEC isochrone (at a distance of 1.99 Mpc) is overlaid in orange.

4.3. Structural Parameters

To measure the underlying structural parameters of Pavo, we fit an exponential profile to the two-dimensional distribution of stars consistent with the RGB using a maximum-likelihood technique (Martin et al. 2008), as implemented in Sand et al. (2012). We selected RGB stars using a color–magnitude selection region within 2σ (photometric uncertainties) of an ancient (10 Gyr) and very metal-poor ([M/H] = −2.5) PARSEC RGB isochrone. This isochrone is shown in orange in most panels of Figure 3. The top right panel shows stars from the NW region of Pavo (orange

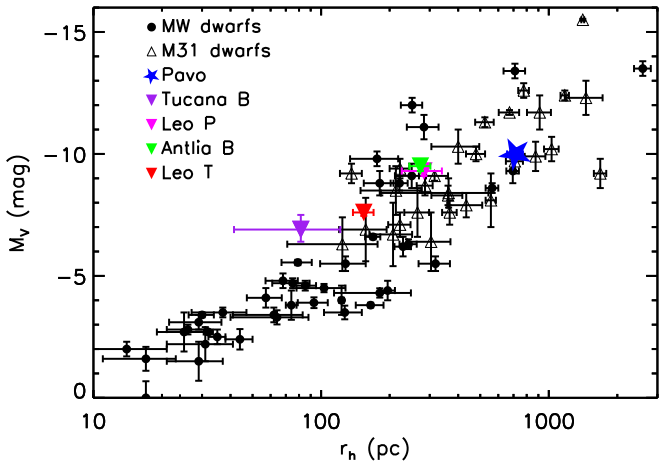

Figure 4. Pavo on the size–luminosity relation with various other Local Volume dwarfs included for comparison. Note that Pavo is at the upper limit of the scatter in effective radius (for its magnitude), while all of the highlighted comparison dwarfs are at the lower limit of the scatter.

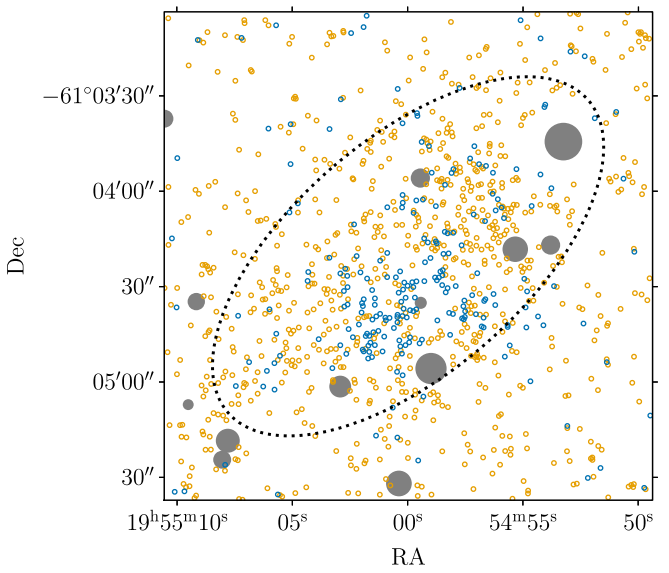

Figure 5. Map of the positions of blue, $g - r < 0$ (blue points), and RGB (orange points) stars (both) brighter than $m_r = 26$. The gray points show the locations of bright stars from Gaia DR3 ($m_G < 19.5$) with point sizes scaled by apparent brightness. The dashed black ellipse indicates the half-light radius of Pavo (Table 1). It is the same ellipse as in Figure 2.

dashed ellipse in Figure 2) compared to this isochrone. Applying this photometric selection across the whole IMACS field yielded our input RGB catalog for our structural analysis. Only stars brighter than $r = 26.5$ mag were included in our selection.

The exponential profile fit includes the central position, position angle (θ), ellipticity (ϵ), half-light radius (r_h), and constant background surface density as free parameters. The algorithm accounts for saturated foreground stars and other regions where Pavo stars could not be detected. Uncertainties were calculated through a bootstrap resampling analysis using 1000 iterations. As a check, we also repeated the calculations while only including RGB stars down to $r = 25.5$ mag; the derived structural parameters agreed within the uncertainties.

The results of the structural analysis can be seen in Table 1, and Pavo is placed on the size–luminosity relation for dwarf galaxies in Figure 4. Pavo is a close match in luminosity to both Leo P and the gas-rich dwarf Antlia B (Sand et al. 2015) but is several times larger. However, all three dwarfs still fall within the scatter of the size–luminosity relation of LG dwarfs.

4.4. Stellar Population

To further investigate the red and blue stellar populations in Pavo, we selected blue stars to contrast with the RGB population from Section 4.3. To do this, we adopted a simple selection criterion of $g - r < 0$. The positions of the red and blue populations are plotted in Figure 5. In both cases, we plot only stars brighter than $m_r = 26$. There are holes in the distribution of stars in certain places due to bright foreground stars or background galaxies. The former are highlighted in Figure 5 with gray circles. For the latter, we simply note that the largest gaps are in the lower left (SE) of Figure 5 due to bright background early- and late-type galaxies (see Figure 2).

From Figure 5, we can clearly see that the NW side of Pavo is dominated by RGB stars, while the south is dominated by blue stars. In both cases, there is a clear overdensity of stars relative to the background, and the majority of this overdensity is encompassed by the ellipse in Figure 5 that was also used to produce the CMD in Figure 3 (top left).

As discussed in Section 4.2, the red stellar population in the NW of Pavo is consistent with being an ancient metal-poor RGB at ∼2 Mpc. This is seen even more clearly in the Hess diagram (with 0.1 mag bins) in Figure 3 (bottom middle), where the RGB isochrone follows the densest parts of the CMD, while overlapping an underdensity in the background CMD (bottom right).

We briefly considered the possibility that this red population might instead be merely the red side of the helium-burning (HeB) branch, with the blue population being the blue side of the branch (and the top of the main sequence of the youngest stars). However, the fact that the two populations can be spatially separated (e.g., Figure 5 and the top right panel of Figure 3) refutes this notion. In addition, a relatively high metallicity (for an object of this luminosity) of $[M/H] \approx -1$ would be required to match the observed colors of the two populations.

In the case of the blue population, the isochrones in Figure 3 (top left) indicate that it is consistent with a combination of main-sequence and HeB stars that are 150–500 Myr old (at 2 Mpc). The metallicity for these isochrones was chosen to approximately match that of Leo P, as we currently have no metallicity estimate for Pavo. The CMD therefore indicates that there was some star formation at least as recently as 150 Myr ago; however, when considering the brightest and bluest stars, we are dealing with small number statistics, and it is possible that Pavo contains some younger stars.

Our Hα observations (Section 3.2) revealed no H II regions, also supporting the notion that there are no very young stars (<10 Myr). However, we note that this does not mean Pavo has completely stopped forming stars. Star formation in these extremely low mass galaxies is highly stochastic and will not evenly sample the full initial mass function (IMF) at any given time. It may be possible that new stars have formed in the past 10 Myr, but none of them are O stars; thus, there are no H II regions. For comparison, Leo P has a single H II region that probably contains only a single O star (Rhode et al. 2013).

To assess this more quantitatively, we consider that the Swift UV detection of Pavo indicates that over the past ∼200 Myr it has had an average SFR of $\sim 1 \times 10^{-4}\, M_* \,\mathrm{yr}^{-1}$. Assuming this

SFR, Pavo might have formed 1000 $M_\odot$ of stars in the past 10 Myr. We used PARSEC to generate 800 realizations of a 1000 $M_\odot$, 10 Myr old single stellar population (with a Kroupa IMF). Every realization contained at least one O star, suggesting that the lack of Hα emission, even at these low masses, implies that there has been a cessation of star formation for at least the past 10 Myr. Another possibility is that the IMF may be top-light, which has been suggested is expected for metal-poor systems with low SFRs (Pflamm-Altenburg & Kroupa 2009; Jeřábková et al. 2018). If this were the case for Pavo, then it is possible that star formation is still proceeding, but there are no stars massive enough to form H II regions. Overall, the simplest explanation is likely that star formation in Pavo proceeds quasi-episodically, and we are currently witnessing a temporary low.

Space-based observations of Pavo will have the depth and resolution to better resolve its stellar population. This will provide considerably more information on the recent star formation, revealing if Pavo has indeed been forming stars in episodic bursts or if its SFR has been largely steady. This will give a clearer indication of whether we are witnessing a temporary lull in SFR or the beginning of a permanent shutdown.

4.5. Stellar and Gas Masses

To estimate the stellar mass of Pavo, we performed aperture photometry (Table 1) on the DECaLS g, r, z, and i, masking clear foreground stars. The stellar mass was estimated using five different magnitude and color scaling relations (based on r- and i-band magnitudes and $g-r$ and $g-i$ colors) from Zibetti et al. (2009), Taylor et al. (2011), and Du & McGaugh (2020). The median value, $\log M_*/M_\odot = 5.6$, was adopted as our stellar mass estimate, and the standard deviation between the five methods, 0.2 dex, was used as the uncertainty (note that this does not include distance uncertainty). This mass is identical within the uncertainty to that of Leo P, $\log M_*/M_\odot = 5.7$ (McQuinn et al. 2015b).

We extracted an H I spectrum at the position of Pavo from the H I Parkes All Sky Survey (HIPASS; Barnes et al. 2001) spectral server[14] but could not identify any significant emission peaks that might correspond to its neutral gas content. There is an $\sim 2\sigma$ peak at approximately $cz_\odot = 1000$ km s^{-1}; however, unless Pavo has a particularly large peculiar velocity (e.g., >500 km s^{-1}), it is unlikely that this peak, if real, is associated. It is also possible that the velocity of Pavo is sufficiently small that any H I emission is overwhelmed by that of the MW. Without dismissing this possibility, if we assume that Pavo's radial velocity is sufficiently large to not be blended with the H I emission of the MW (e.g., $cz_\odot \gtrsim 100$ km s^{-1} for this region of the sky), we can estimate an upper limit for its H I mass based on the HIPASS spectrum. This spectrum has an rms noise of 8.2 mJy (13 km s^{-1} resolution). If we assume a velocity width of 30 km s^{-1} for Pavo (Leo P's H I velocity width is 24 km s^{-1}; Giovanelli et al. 2013), then at 2 Mpc, this translates to a 3σ upper limit on Pavo's H I mass of $\log M_{\rm H\,I}/M_\odot < 6.0$. We note that the H I mass of Leo P, $\log M_*/M_\odot = 5.9$ (Giovanelli et al. 2013; McQuinn et al. 2015b), would be marginally below this limit.

If we go further and assume that the radial velocity of Pavo is in the range of 100–500 km s^{-1}, we can also use the Galactic All-Sky Survey (GASS; McClure-Griffiths et al. 2009; Kalberla & Haud 2015) to constrain Pavo's H I mass. We inspected a spectral cube from GASS[15] but found no sign of H I line emission from Pavo. The rms noise in this cube was 49 mK at 1 km s^{-1} resolution. Using 0.7 K Jy^{-1} as the approximate gain of the Parkes radio telescope, this translates to a 3σ upper limit on the H I mass of Pavo of $\log M_{\rm H\,I}/M_\odot < 5.6$. Although this limit is slightly lower than that from HIPASS, the previous limit is stricter in the sense that it does not assume an upper limit of 500 km s^{-1} for the radial velocity of Pavo.

Although it is unclear if Pavo currently contains a significant gas reservoir, it must have done so recently in order to explain its population of young stars. Giovanelli & Haynes (2015) suggested that very low mass, star-forming galaxies, such as Pavo and Leo P, might periodically become invisible to H I surveys if feedback ejects much of their gas reservoirs. Recent simulations of galaxies in this mass range (Rey et al. 2020, 2022) support this hypothesis. Thus, it may be that Pavo's apparent lull in SFR is also reflected in its gas content. However, deeper H I observations are need to confirm/refute this possibility.

4.6. Environment

Figure 6 shows two projections (in Cartesian supergalactic coordinates) of nearby galaxies (from Karachentsev & Kaisina 2019). We have highlighted Pavo, as well as Tucana B and Leo P, for the purpose of comparison. Pavo is slightly further from the MW than either Tucana B or Leo P and, in fact, is remarkably isolated. Figure 6 shows that Pavo is part of the local sheet and in a direction away from any known nearby group/structure. In three dimensions, the nearest neighbor to Pavo (in the catalog of Karachentsev & Kaisina 2019) is IC 5152, over 600 kpc away. This makes it even more isolated than Leo P, which is already regarded as a pristine object that likely has never entered the virial radius of a more massive system (Giovanelli et al. 2013).

5. Discussion

The exceptional isolation of Pavo makes it an ideal candidate for follow-up observations to understand how star formation proceeds in the lowest-mass star-forming galaxies. Upcoming space-based observations (HST-GO-17514; PI: B. Mutlu-Pakdil) will be capable of resolving its stellar population, even in the brightest clumps where our IMACS data become too crowded (Figure 5), and trace both the main sequence and RGB down to fainter magnitudes. Fitting star formation histories to these deeper CMDs (see McQuinn et al. 2015a) would indicate whether Pavo has been continuously forming stars since before reionization, formed stars episodically, or perhaps only recently revived its star formation after having been quenched at high redshift.

Although we have compared Pavo to Leo P and Tucana B throughout this work, we note that there really is no other known galaxy that is a close match for all of Pavo's properties. Tucana B is clearly not morphologically similar to Pavo, but we used it as a point of comparison because Tucana B is currently the only known isolated UFD. Presumably, if Pavo were several times less massive, its gas reservoir would not

[14] https://www.atnf.csiro.au/research/multibeam//release/

[15] https://www.astro.uni-bonn.de/hisurvey/gass/index.php

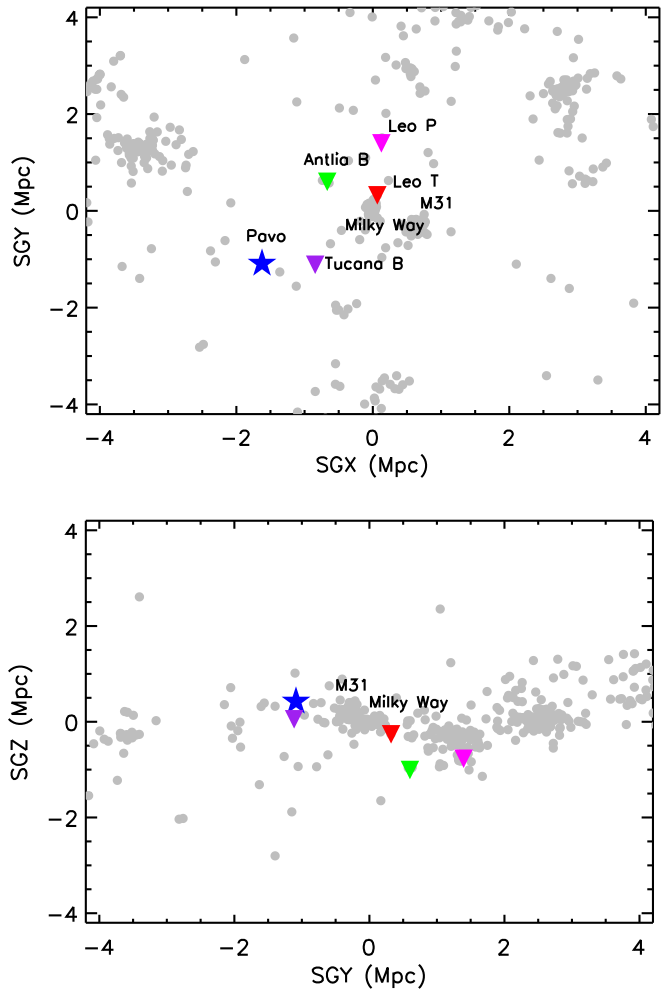

Figure 6. Supergalactic *XY* (top) and *YZ* (bottom) projections showing objects in the nearby galaxies catalog (Karachentsev & Kaisina 2019). Pavo is shown with a blue star. Several other notable dwarf galaxies that we refer to are highlighted for comparison.

have survived reionization, and today it would appear more like Tucana B. Pavo and Leo P are morphologically similar and appear to have similar stellar populations, but the spatial extent of Pavo's RGB stars is roughly fives times larger than that of Leo P's, indicating that it is quite a different object. The close similarity of the physical properties of Antlia B and Leo P (e.g., Figure 4), while one is close to a massive galaxy and the other is isolated, suggests that relative isolation is unlikely to be the root cause of Pavo's more extended stellar population and that instead, there is probably an underlying, intrinsic cause. What the lack of close comparisons for Pavo really highlights is the dearth of isolated galaxies that are known in this mass regime. Building a better understanding of these objects and determining observationally where the tipping point between objects like Pavo and Tucana B occurs will require a statistical sample of isolated dwarfs (both quenched and star-forming) in this mass regime ($M_* \lesssim 10^6\ M_\odot$).

Exceptionally low mass, star-forming galaxies such as Pavo and Leo P trace the boundary of galaxy mass needed to survive cosmic reionization and continue forming stars. Tollerud & Peek (2018) used the transitional dwarf Leo T, $\log L_V/L_\odot = 5.1$ and $D = 0.42$ Mpc (Irwin et al. 2007), to place an approximate upper limit on this mass scale. However, just above the mass of Leo T, there should be an abundance of Leo P analogs just outside the LG. We posit that Pavo is merely the first such analog to be identified. By building up this sample, as well as a sample of field UFDs (e.g., Tucana B analogs), we can constrain the mass threshold to survive reionization from both sides without the complication of interactions with a host galaxy.

In the next few years, new wide-field H I surveys, currently in progress, will undoubtedly uncover new analogous star-forming dwarfs. In particular, the Commensal Radio Astronomy FasT Survey (Zhang et al. 2021) with the Five hundred meter Aperture Spherical Telescope and the Widefield ASKAP *L*-band Legacy All-sky Blind surveY (Koribalski et al. 2020) will together cover almost the entire sky to at least the sensitivity of ALFALFA (several times deeper than HIPASS). These H I surveys will pick out any Leo P analogs and, at slightly higher masses, greatly expand on the SHIELD sample. However, as these surveys will only be sensitive to gas-bearing galaxies that have fuel for star formation (and that therefore likely contain young, blue stars), many of the objects that they will uncover in this regime are likely already identifiable in Legacy Survey images, if they are searched for with a suitably optimized approach. Pavo may be the first such object to have been identified, but there are undoubtedly many more.

At optical and infrared wavelengths, the upcoming Rubin Legacy Survey of Space and Time (LSST) and the Nancy Grace Roman High Latitude Wide Area Survey will provide unprecedented opportunities to identify nearby, isolated, and very low mass dwarf galaxies. Resolved star searches will be an effective tool with LSST out to a few megaparsecs (e.g., Mutlu-Pakdil et al. 2021), while for Roman, this technique will be viable out to ∼10 Mpc (but over a much smaller survey area). However, as our discovery of Pavo has demonstrated, this distance range can be readily extended by incorporating machine learning–aided classification in the semiresolved regime. As the accessible survey volume grows like the cube of distance, even increasing this maximum distance by a small factor represents a major gain in terms of the number of identifiable sources.

In subsequent papers, we will present the full sample of candidate analogs to Leo P, SHIELD galaxies, and Tucana B that we have uncovered in our machine learning–aided search of the DESI legacy imaging surveys. Further developing and optimizing this technique will allow semiresolved nearby dwarf galaxies to be identified not just in existing imaging surveys but also in upcoming next-generation surveys, such as LSST and Roman, and maximize their potential for extragalactic science at the lowest masses.

Acknowledgments

We thank the anonymous referee for the rapid and helpful response. This work used images from the Dark Energy Camera Legacy Survey (DECaLS; Proposal ID 2014B-0404; PIs: David Schlegel and Arjun Dey). Full acknowledgment is at https://www.legacysurvey.org/acknowledgment/. Based on observations obtained at the Southern Astrophysical Research (SOAR) telescope, which is a joint project of the Ministério da Ciência, Tecnologia e Inovações (MCTI/LNA) do Brasil, the US National Science Foundation's NOIRLab, the University of North Carolina at Chapel Hill (UNC), and Michigan State University (MSU). This publication uses data generated via the Zooniverse.org platform, development of which is funded by generous support, including a Global Impact Award from

Google, and by a grant from the Alfred P. Sloan Foundation. D. J.S. acknowledges support from NSF grants AST-1821967, 1813708, and AST-2205863. Research by D.C. is supported by NSF grant AST-1814208. K.S. acknowledges support from the Natural Sciences and Engineering Research Council of Canada (NSERC). J.S. acknowledges support from the Packard Foundation. A.K. acknowledges support from NSERC, the University of Toronto Arts & Science Postdoctoral Fellowship program, and the Dunlap Institute. D.Z. and R.D. acknowledge support from NSF AST-2006785 and NASA ADAP 80NSSC23K0471 for their work on the SMUDGes pipeline.

Facilities: Blanco, Magellan:Baade (IMACS), SOAR, Swift, Parkes, Gaia.

Software: `astrometry.net`[16] (Lang et al. 2010), `SCAMP`[17] (Bertin 2006), `SWarp`[18] (Bertin et al. 2002), `astropy`[19] (Astropy Collaboration et al. 2013, 2018), `Photutils`[20] (Bradley et al. 2020), `reproject`[21] (Robitaille et al. 2020), `matplotlib`[22] (Hunter 2007), `numpy`[23] (van der Walt et al. 2011), `scipy`[24] (Oliphant 2007; Millman & Aivazis 2011), `pandas`[25] (McKinney 2010; pandas development team 2020), `astroquery`[26] (Ginsburg et al. 2019), `astroalign`[27] (Beroiz et al. 2020), ccdproc[28] (Craig et al. 2017), `DS9`[29] (Joye & Mandel 2003), `GALFIT`[30] (Peng et al. 2002, 2010), `daophot`, and `allframe` (Stetson 1987, 1994).

ORCID iDs

Michael G. Jones https://orcid.org/0000-0002-5434-4904
Burçin Mutlu-Pakdil https://orcid.org/0000-0001-9649-4815
David J. Sand https://orcid.org/0000-0003-4102-380X
Richard Donnerstein https://orcid.org/0000-0001-7618-8212
Denija Crnojević https://orcid.org/0000-0002-1763-4128
Paul Bennet https://orcid.org/0000-0001-8354-7279
Catherine E. Fielder https://orcid.org/0000-0001-8245-779X
Ananthan Karunakaran https://orcid.org/0000-0001-8855-3635
Kristine Spekkens https://orcid.org/0000-0002-0956-7949
Jay Strader https://orcid.org/0000-0002-1468-9668
Ryan Urquhart https://orcid.org/0000-0003-1814-8620
Dennis Zaritsky https://orcid.org/0000-0002-5177-727X

References

Astropy Collaboration, Price-Whelan, A. M., Sipőcz, B. M., et al. 2018, AJ, 156, 123
Astropy Collaboration, Robitaille, T. P., Tollerud, E. J., et al. 2013, A&A, 558, A33
Bailer-Jones, C. A. L., Rybizki, J., Fouesneau, M., Demleitner, M., & Andrae, R. 2021, AJ, 161, 147
Barnes, D. G., Staveley-Smith, L., de Blok, W. J. G., et al. 2001, MNRAS, 322, 486
Belokurov, V., Zucker, D. B., Evans, N. W., et al. 2006, ApJL, 647, L111
Bennet, P., Sand, D. J., Crnojević, D., et al. 2019, ApJ, 885, 153
Benson, A. J., Frenk, C. S., Lacey, C. G., Baugh, C. M., & Cole, S. 2002, MNRAS, 333, 177
Beroiz, M., Cabral, J., & Sanchez, B. 2020, A&C, 32, 100384
Bertin, E. 2006, in ASP Conf. Ser. 351, Astronomical Data Analysis Software and Systems XV, ed. C. Gabriel et al. (San Francisco, CA: ASP), 112
Bertin, E., Mellier, Y., Radovich, M., et al. 2002, in ASP Conf. Ser. 281, Astronomical Data Analysis Software and Systems XI, ed. D. A. Bohlender, D. Durand, & T. H. Handley (San Francisco, CA: ASP), 228
Bovill, M. S., & Ricotti, M. 2009, ApJ, 693, 1859
Boylan-Kolchin, M., Bullock, J. S., & Kaplinghat, M. 2011, MNRAS, 415, L40
Bradley, L., Sipőcz, B., Robitaille, T., et al. 2020, astropy/photutils: v1.0.0, Zenodo, doi:10.5281/zenodo.4044744
Bressan, A., Marigo, P., Girardi, L., et al. 2012, MNRAS, 427, 127
Brook, C. B., & Di Cintio, A. 2015, MNRAS, 450, 3920
Bullock, J. S., & Boylan-Kolchin, M. 2017, ARA&A, 55, 343
Cannon, J. M., Giovanelli, R., Haynes, M. P., et al. 2011, ApJL, 739, L22
Carlin, J. L., Mutlu-Pakdil, B., Crnojević, D., et al. 2021, ApJ, 909, 211
Carlin, J. L., Sand, D. J., Price, P., et al. 2016, ApJL, 828, L5
Cerny, W., Martínez-Vázquez, C. E., Drlica-Wagner, A., et al. 2023, ApJ, 953, 1
Cerny, W., Pace, A. B., Drlica-Wagner, A., et al. 2021, ApJL, 920, L44
Chiboucas, K., Jacobs, B. A., Tully, R. B., & Karachentsev, I. D. 2013, AJ, 146, 126
Chiti, A., Frebel, A., Jerjen, H., Kim, D., & Norris, J. E. 2020, ApJ, 891, 8
Clemens, J. C., Crain, J. A., & Anderson, R. 2004, Proc. SPIE, 5492, 331
Collins, M. L. M., Charles, E. J. E., Martínez-Delgado, D., et al. 2022, MNRAS, 515, L72
Craig, M., Crawford, S., Seifert, M., et al. 2017, astropy/ccdproc: v1.3.0.post1, Zenodo, doi:10.5281/zenodo.1069648
Crnojević, D., Sand, D. J., Bennet, P., et al. 2019, ApJ, 872, 80
Crnojević, D., Sand, D. J., Caldwell, N., et al. 2014, ApJL, 795, L35
Crnojević, D., Sand, D. J., Spekkens, K., et al. 2016, ApJ, 823, 19
Da Costa, G. S., & Armandroff, T. E. 1990, AJ, 100, 162
Dey, A., Schlegel, D. J., Lang, D., et al. 2019, AJ, 157, 168
Dressler, A., Hare, T., Bigelow, B. C., & Osip, D. J. 2006, Proc. SPIE, 6269, 62690F
Drlica-Wagner, A., Bechtol, K., Rykoff, E. S., et al. 2015, ApJ, 813, 109
Drlica-Wagner, A., Carlin, J. L., Nidever, D. L., et al. 2021, ApJS, 256, 2
Du, W., & McGaugh, S. S. 2020, AJ, 160, 122
Dutton, A. A., Macciò, A. V., Frings, J., et al. 2016, MNRAS, 457, L74
Fitts, A., Boylan-Kolchin, M., Elbert, O. D., et al. 2017, MNRAS, 471, 3547
Gaia Collaboration, Prusti, T., de Bruijne, J. H. J., et al. 2016, A&A, 595, A1
Gaia Collaboration, Vallenari, A., Brown, A. G. A., et al. 2023, A&A, 674, A1
Garrison-Kimmel, S., Wetzel, A., Bullock, J. S., et al. 2017, MNRAS, 471, 1709
Ginsburg, A., Sipőcz, B. M., Brasseur, C. E., et al. 2019, AJ, 157, 98
Giovanelli, R., & Haynes, M. P. 2015, A&ARv, 24, 1
Giovanelli, R., Haynes, M. P., Adams, E. A. K., et al. 2013, AJ, 146, 15
Giovanelli, R., Haynes, M. P., Kent, B. R., et al. 2005, AJ, 130, 2598
Haynes, M. P., Giovanelli, R., Kent, B. R., et al. 2018, ApJ, 861, 49
Hoversten, E. A., Gronwall, C., Vanden Berk, D. E., et al. 2009, ApJ, 705, 1462
Hunter, J. D. 2007, CSE, 9, 90
Iglesias-Páramo, J., Buat, V., Takeuchi, T. T., et al. 2006, ApJS, 164, 38
Irwin, M. J., Belokurov, V., Evans, N. W., et al. 2007, ApJL, 656, L13
Jeřábková, T., Hasani Zonoozi, A., Kroupa, P., et al. 2018, A&A, 620, A39
Joye, W. A., & Mandel, E. 2003, in ASP Conf. Ser. 295, Astronomical Data Analysis Software and Systems XII, ed. H. E. Payne, R. I. Jedrzejewski, & R. N. Hook (San Francisco, CA: ASP), 489
Kalberla, P. M. W., & Haud, U. 2015, A&A, 578, A78
Karachentsev, I. D., & Kaisina, E. I. 2019, AstBu, 74, 111
Klypin, A., Kravtsov, A. V., Valenzuela, O., & Prada, F. 1999, ApJ, 522, 82
Koposov, S. E., Belokurov, V., Torrealba, G., & Evans, N. W. 2015, ApJ, 805, 130
Koribalski, B. S., Staveley-Smith, L., Westmeier, T., et al. 2020, Ap&SS, 365, 118

[16] http://astrometry.net/
[17] https://www.astromatic.net/software/scamp/
[18] https://www.astromatic.net/software/swarp/
[19] https://www.astropy.org/index.html
[20] https://photutils.readthedocs.io/en/stable/
[21] https://reproject.readthedocs.io/en/stable/
[22] https://matplotlib.org/
[23] https://numpy.org/
[24] https://scipy.org/
[25] https://pandas.pydata.org/
[26] https://astroquery.readthedocs.io/en/latest/
[27] https://astroalign.quatrope.org/en/latest/
[28] https://ccdproc.readthedocs.io/en/latest/
[29] https://sites.google.com/cfa.harvard.edu/saoimageds9
[30] https://users.obs.carnegiescience.edu/peng/work/galfit/galfit.html

Lang, D., Hogg, D. W., Mierle, K., Blanton, M., & Roweis, S. 2010, AJ, 139, 1782
Lee, M. G., Freedman, W. L., & Madore, B. F. 1993, ApJ, 417, 553
Makarov, D., Makarova, L., Rizzi, L., et al. 2006, AJ, 132, 2729
Martin, N. F., de Jong, J. T. A., & Rix, H.-W. 2008, ApJ, 684, 1075
Martínez-Delgado, D., Karim, N., Charles, E. J. E., et al. 2022, MNRAS, 509, 16
McClure-Griffiths, N. M., Pisano, D. J., Calabretta, M. R., et al. 2009, ApJS, 181, 398
McConnachie, A. W., Huxor, A., Martin, N. F., et al. 2008, ApJ, 688, 1009
McGaugh, S. S. 2012, AJ, 143, 40
McKinney, W. 2010, in Proc. 9th Python in Science Conf., ed. S. van der Walt & J. Millman, 56
McNanna, M., Bechtol, K., Mau, S., et al. 2023, arXiv:2309.04467
McQuinn, K. B. W., Cannon, J. M., Dolphin, A. E., et al. 2014, ApJ, 785, 3
McQuinn, K. B. W., Cannon, J. M., Dolphin, A. E., et al. 2015a, ApJ, 802, 66
McQuinn, K. B. W., Mao, Y.-Y., Cohen, R. E., et al. 2023, arXiv:2307.08738
McQuinn, K. B. W., Skillman, E. D., Dolphin, A., et al. 2015b, ApJ, 812, 158
Millman, K. J., & Aivazis, M. 2011, CSE, 13, 9
Moore, B. 1994, Natur, 370, 629
Müller, O., Rejkuba, M., Pawlowski, M. S., et al. 2019, A&A, 629, A18
Mutlu-Pakdil, B., Sand, D. J., Carlin, J. L., et al. 2018, ApJ, 863, 25
Mutlu-Pakdil, B., Sand, D. J., Crnojević, D., et al. 2021, ApJ, 918, 88
Mutlu-Pakdil, B., Sand, D. J., Crnojević, D., et al. 2022, ApJ, 926, 77
Oliphant, T. E. 2007, CSE, 9, 10
pandas development team, T 2020, pandas-dev/pandas: Pandas, v1.2.5, Zenodo, doi:10.5281/zenodo.3509134
Pawlowski, M. S., Pflamm-Altenburg, J., & Kroupa, P. 2012, MNRAS, 423, 1109
Peng, C. Y., Ho, L. C., Impey, C. D., & Rix, H.-W. 2002, AJ, 124, 266
Peng, C. Y., Ho, L. C., Impey, C. D., & Rix, H.-W. 2010, AJ, 139, 2097
Pflamm-Altenburg, J., & Kroupa, P. 2009, ApJ, 706, 516
Rey, M. P., Pontzen, A., Agertz, O., et al. 2020, MNRAS, 497, 1508
Rey, M. P., Pontzen, A., Agertz, O., et al. 2022, MNRAS, 511, 5672
Rhode, K. L., Salzer, J. J., Haurberg, N. C., et al. 2013, AJ, 145, 149
Robitaille, T., Deil, C., & Ginsburg, A., 2020 reproject: Python-based Astronomical Image Reprojection, Astrophysics Source Code Library, ascl:2011.023
Sales, L. V., Wetzel, A., & Fattahi, A. 2022, NatAs, 6, 897
Sánchez, E. & Des Collaboration 2010, JPhCS, 259, 012080
Sand, D. J., Crnojević, D., Strader, J., et al. 2014, ApJL, 793, L7
Sand, D. J., Mutlu-Pakdil, B., Jones, M. G., et al. 2022, ApJL, 935, L17
Sand, D. J., Spekkens, K., Crnojević, D., et al. 2015, ApJL, 812, L13
Sand, D. J., Strader, J., Willman, B., et al. 2012, ApJ, 756, 79
Sawala, T., Frenk, C. S., Fattahi, A., et al. 2016, MNRAS, 457, 1931
Schlafly, E. F., & Finkbeiner, D. P. 2011, ApJ, 737, 103
Schlegel, D. J., Finkbeiner, D. P., & Davis, M. 1998, ApJ, 500, 525
Simon, J. D. 2019, ARA&A, 57, 375
Simpson, C. M., Bryan, G. L., Johnston, K. V., et al. 2013, MNRAS, 432, 1989
Smercina, A., Bell, E. F., Price, P. A., et al. 2018, ApJ, 863, 152
Smercina, A., Bell, E. F., Slater, C. T., et al. 2017, ApJL, 843, L6
Stetson, P. B. 1987, PASP, 99, 191
Stetson, P. B. 1994, PASP, 106, 250
Taylor, E. N., Hopkins, A. M., Baldry, I. K., et al. 2011, MNRAS, 418, 1587
Tollerud, E. J., & Peek, J. E. G. 2018, ApJ, 857, 45
van der Walt, S., Colbert, S. C., & Varoquaux, G. 2011, CSE, 13, 22
Wetzel, A. R., Hopkins, P. F., Kim, J.-h., et al. 2016, ApJL, 827, L23
Wheeler, C., Oñorbe, J., Bullock, J. S., et al. 2015, MNRAS, 453, 1305
Willman, B., Dalcanton, J. J., Martinez-Delgado, D., et al. 2005, ApJL, 626, L85
York, D. G., Anderson, J., Anderson, J. E. J., et al. 2000, AJ, 120, 1579
Zaritsky, D., Donnerstein, R., Dey, A., et al. 2019, ApJS, 240, 1
Zaritsky, D., Donnerstein, R., Dey, A., et al. 2023, ApJS, 267, 27
Zaritsky, D., Donnerstein, R., Karunakaran, A., et al. 2021, ApJS, 257, 60
Zaritsky, D., Donnerstein, R., Karunakaran, A., et al. 2022, ApJS, 261, 11
Zhang, K., Wu, J., Li, D., et al. 2021, MNRAS, 500, 1741
Zibetti, S., Charlot, S., & Rix, H.-W. 2009, MNRAS, 400, 1181